SUPPORTING INFORMATION

Colossal expansion and fast motion in spin-crossover@polymer actuators

Mario Piedrahita-Bello,[1,2] José Elias Angulo Cervera,[1,2] Alejandro Enriquez-Cabrera[1], Gábor Molnár,[1] Bertrand Tondu,[2] Lionel Salmon,[1,*] Azzedine Bousseksou[1,*]

[1]LCC, CNRS & Université de Toulouse (UPS, INP), 31077 Toulouse, France

[2]LAAS, CNRS & Université de Toulouse (UPS, INSA), 31400 Toulouse, France

Lionel.salmon@lcc-toulouse.fr, azzedine.bousseksou@lcc-toulouse.fr

A-Methods

1-Synthesis of ligands and spin crossover complexes

All solvents and reagents were purchased from Sigma Aldrich and used without further purification. Synthesis of the 4-pentyl-1,2,4-triazole (C_5trz) ligand was performed using the following procedure: 2.6 g (43.14 mmol) of monoformyl hydrazine was dissolved in 100 mL of ethanol and 7.6 mL (45.73 mmol) of triethyl orthoformate was added slowly. The mixture was refluxed for 4 h and then cooled to room temperature. 5 mL (43.14 mmol) of amylamine was added and the reaction was kept in reflux for 20 h. The product was cooled to room temperature and dried by vacuum, with a yellow oil as product. The product was diluted in 100 mL of dichloromethane and washed with 3 x 15 mL of water, then extracted with 4 x 8 mL of an HCl solution (5 mL of conc. HCl + 3 mL of H_2O). The acid solution was then carefully neutralized with NaOH to pH 7-8 and then the product was extracted with 4 x 20 mL of dichloromethane. The final solution of dichloromethane was then dried with $MgSO_4$ and then evaporated to dryness resulting in 2.8 g (68%) of a slight yellow oil as a pure product. ^{1}H NMR (300 MHz, $CDCl_3$) δ 8.13 (s, 2H), 3.99 (t, J = 7.2 Hz, 2H), 1.78 (p, J = 7.4 Hz, 2H), 1.42 – 1.17 (m, 4H), 0.86 (t, J = 7.0 Hz, 3H). ^{13}C NMR (75 MHz, $CDCl_3$) δ 142.7, 45.3, 30.4, 28.4, 22.0, 13.7.

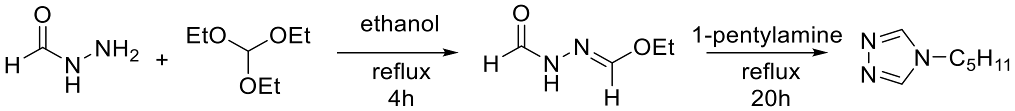

Scheme1: Synthesis of the 4-pentyl-1,2,4-triazole (C_5trz) ligand

Synthesis of the 4-octadeyl-1,2,4-triazole ligand (C_{18}trz) ligand (11.7 g, 82%) was performed in the same conditions using 12 g of stearylamine (82% yield). ^{1}H NMR (300 MHz, $CDCl_3$) δ 8.17 (s, 2H), 4.02 (t, J = 7.2 Hz, 2H), 1.82 (p, J = 6.7, 6.3 Hz, 2H), 1.41 – 1.15 (m, 30H), 1.01 – 0.76 (m, 3H). ^{13}C NMR (75 MHz, $CDCl_3$) δ 142.7, 45.4, 31.9, 30.7, 29.7, 29.6, 29.6, 29.5 29.5, 29.3, 28.9, 26.4, 22.7, 14.1.

The $[Fe(C_n trz)_3](OTs)_2$ (**1** and **2**) complexes were synthesized according to a slightly modified method from the reference : O. Roubeau, et al. New J. Chem., 2001, 25, 144-150.

$[Fe(C_5 trz)_3](OTs)_2$ (**1**) was synthesized dissolving 750 mg (5.38 mmol) of the 4-pentyl-1,2,4-triazol in 25 mL of ethanol. In a separated flask 909 mg (1.79 mmol) of the $Fe(OTs)_2{\cdot}6H_2O$ was dissolved in 25 mL of water with some ascorbic acid. The iron solution was added slowly to the triazole ligand solution, and the mixture was stirred for 24 hours at room temperature resulting in a pink precipitate. The pink product was filtrated under vacuum and then washed with water, ethanol and diethyl ether; resulting in 900 mg of a pink solid (56% yield). Elemental analyses calculated for $[Fe(C_5H_{11}trz)_3](OTs)_2{\cdot}4H_2O$: C, 47.4; H, 6.9; N, 14.2%, found: C, 47.6; H, 7.1; N, 14.2%.

$[Fe(C_{18}trz)_3](OTs)_2$ (**2**) was synthesized dissolving 1.5 g (4.66 mmol) of the 4-octadeyl-1,2,4-triazol in 75 mL of ethanol. In a separated flask, 787.3 mg (1.55 mmol) of the $Fe(OTs)_2{\cdot}6H_2O$ was dissolved in 75 mL of distilled water with some ascorbic acid. The iron solution was added slowly to the triazole ligand solution, and it was stirred like this for 24 h at room temperature resulting in a pink suspension. It was filtrated under vacuum and then washed with water, ethanol and diethyl ether; resulting in 1.56 g of a pink solid (71% yield). Elemental analyses calculated for $[Fe(C_{18}H_{37}trz)_3](Ots)_2{\cdot}2H_2O$: C, 63.5; H, 9.7; N, 9.0%, found: C, 63.4; H, 9.8; N, 8.9%.

The spin crossover complex $[Fe(NH_2trz)]SO_4$ (**3**) was prepared using the following procedure: a solution of 6 g of $FeSO_4{\cdot}7H_2O$ (21.6 mmol) in 12 ml of H_2O was added to 5.46 g of 1,2,4-4-NH_2-triazole (65 mmol) in 12 mL of H_2O. The resulting pink solution was stirred during 36 hours and the pink formed precipitate was purified by three successive ethanol washing/centrifugation cycles (73% yield). Elemental analyses calculated for $[Fe(NH_2trz)]SO_4{\cdot}1H_2O$: C, 17.1; H, 3.3; N, 39.8%, found: C, 17.1; H, 2.6; N,39.8%.

The SCO complex $[Fe(NH_2trz)_3](BF_4)_2$ (**4**) was synthesized using the following procedure: 2.5 mL of a 0.395 M solution of $Fe(BF_4)_2{\cdot}6H2O$ in H_2O was mixed with a solution containing 727 mg of 1,2,4-4-NH_2-triazole in 2.5 mL of H_2O. The mixture was allowed to react for 24 h. The resulting white solid was cleaned multiple times by centrifugation with ethanol and dried under vacuum. (54% yield). Elemental analyses calculated for $[Fe(NH_2trz)_3](BF_4)_2{\cdot}0.3H_2O$: C, 14.8; H, 2.6; N, 34.4%, found: C, 14.9; H, 2.0; N, 34.0%.

Rod-like microparticles of $[Fe(Htrz)_{1.8}(trz)_1(NH_2trz)_{0.2}](BF_4)_1{\cdot}0.7H_2O$ (**5**) were prepared using the following procedure: two equivalent microemulsions were prepared mixing together 3.85 ml of Triton X-100, 3.6 ml of pentanol and 8 ml cyclohexane. To this mixture, a solution of 424 mg of $Fe(BF_4)2{\cdot}6H_2O$ in 2.75 ml H2O was added dropwise to obtain the first microemulsion, whereas a solution of 234 mg of 1,2,4-4-H-triazole and 32 mg of 1,2,4-4-NH_2-triazole (6.6 %) in 2.75 ml H_2O was added to obtain the second microemulsion. These microemulsions were stirred at room temperature until clear solutions were obtained and then quickly mixed together. Several minutes after, the mixture became pink due to the particle formation. The resulting microemulsion was agitated during 24 hours to ensure that the microemulsion exchange was completed. Then, 30 ml ethanol was added to destroy the microemulsion structure. The obtained nanoparticles were washed several times with ethanol to remove the traces of the surfactant and the resulting pink powder (32% yields) was separated by centrifugation (4000 rpm, 10 minutes). Elemental analyses calculated for $[Fe(Htrz)_{1.8}(trz)_1(NH_2trz)_{0.2}](BF_4)_1 \cdot 0.7H_2O$: C, 19.6; H, 2.9; N, 35.1; B, 2.9; Fe, 15.2 found C, 20.3; H, 2.1; N, 32.9; B, 2.7; Fe, 15.2.

Careful tuning of the synthetic conditions was necessary to achieve the highly anisotropic microparticles. In particular, the concentration of the reactants in the aqueous phase and the ω_0 (water to surfactant molar ratio) were of vital importance. Examples of particles of $[Fe(Htrz)_{1.8}(trz)_1(NH_2trz)_{0.2}](BF_4)_1 \cdot 0.7H_2O$ synthesized under various conditions are shown below:

$\omega_0 = 15$ $[Fe^{2+}] = 0{,}27$ M $\omega_0 = 24$ $[Fe^{2+}] = 0{,}22$ M $\omega_0 = 31$ $[Fe^{2+}] = 0{,}19$ M

Figure S1. Representative TEM images of samples of complex $[Fe(Htrz)_{1.8}(trz)_1(NH_2trz)_{0.2}](BF_4)_1 \cdot 0.7H_2O$ synthesized under various conditions.

2-Bilayer device fabrication

The active P(VDF-TrFE)/SCO composite layer films were prepared by dispersing each SCO complex (90 mg) in 2-Butanone (1.8 mL) in an ultrasonic bath for 40 min. Then, the P(VDF-TrFE) 70/30 copolymer (270 mg) was added to the mixture and dissolved at 45 °C to form a 2.16M P(VDF-TrFE) solution in butatone. The resulting suspensions were then blade-cast at a height of 1.50 mm on a heated Teflon surface at 50 °C and kept at this temperature for 10 minutes, until the composite was dry, obtaining in a reproducible manner films of ca 90 µm thickness. The conductive layer was then prepared by dispersing 10 µm Ag flakes (318 mg) in of 2-Butanone (1.8

mL) in an ultrasonic bath for 5 min. Then, the P(VDF-TrFE) copolymer (216 mg) was added to the mixture and dissolved at 45 °C. The resulting suspensions were then blade-cast at a height of 1.5 mm on top of the recently dried active layer at 50 °C and kept at this temperature for ca. 2 h, until the composite was completely dry (Fig. S1) obtaining in a reproducible manner bilayer films of ca 150 µm thickness (ca 60 µm thickness for the conductive layer). The bilayer films were then annealed at 105°C for 12 h. Bilayer devices with size 30 x 20 x 0.15 mm^3 were then cut into a U-shape using a Realmeca RV 2-SP high precision lathe. Control of the thickness of the bilayer was realized with a Mitutoyo precision micrometer all along the 3 cm of the actuators and a mean value of 160 µm was obtained with a standard deviation of 20 µm.

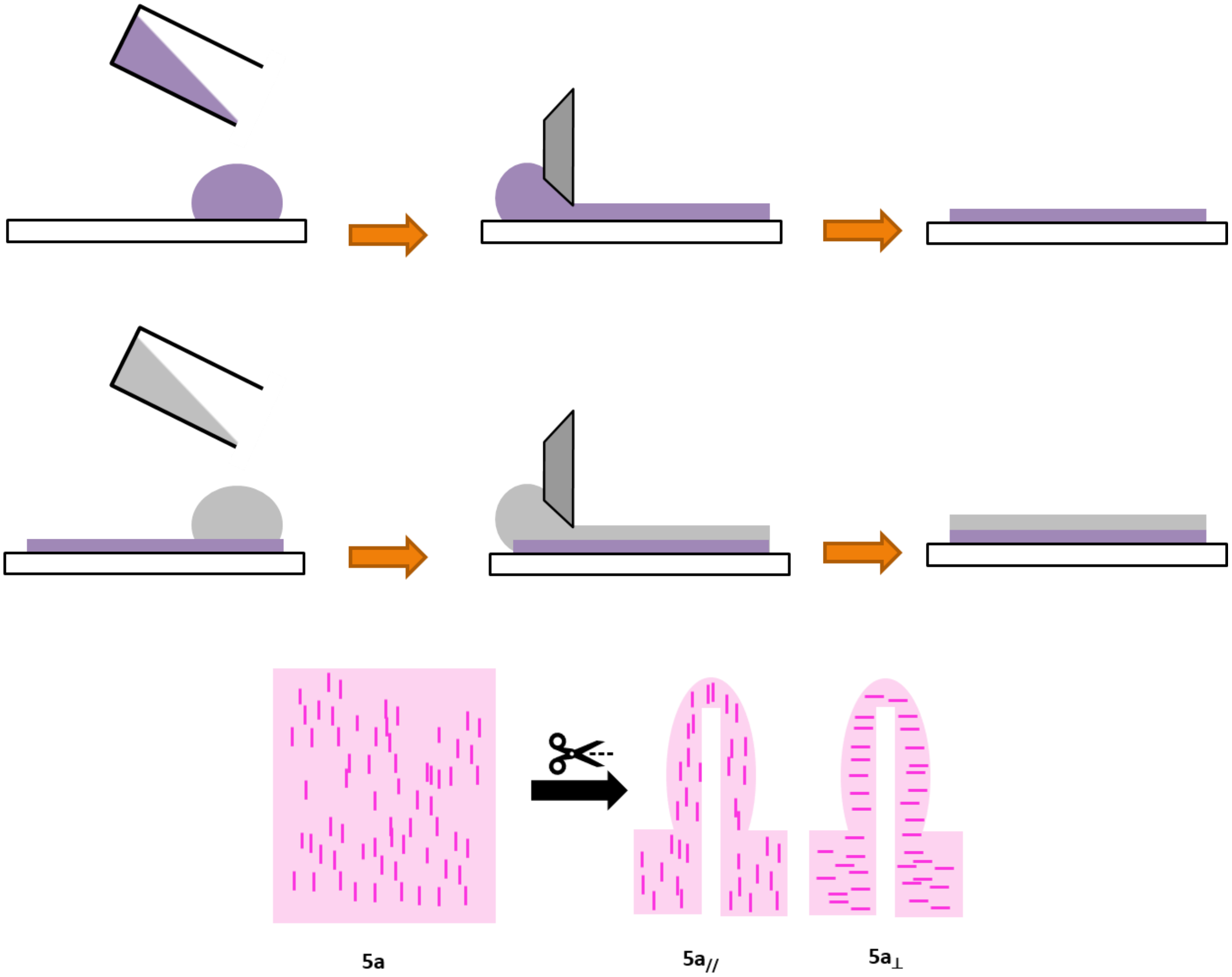

Figure S2. Process for the elaboration of the bilayer devices: blade-casting method and scheme showing the orientation of the cut of anisotropic composite **5a** to obtain samples **5a**$_{//}$ and **5a**$_{\perp}$.

3-Gripper device fabrication

In order to realize the gripper device, three independent SCO bilayer actuators **1a** were fabricated as mentioned here above. The three actuators were then assembled on a plastic piece mounted on a metallic arm. Each actuators were independently electrically connected to a source meter unit embedding electric cables in a thin additional P(VDF-TrFe) layer on the silver containing layer. Here, the aim is to create a soft device that could take an object and displace it to a specific location. As shown in **Figure S3,** each independent actuator is used as a finger of the gripper and can be electrically activated simultaneously to catch and release an object.

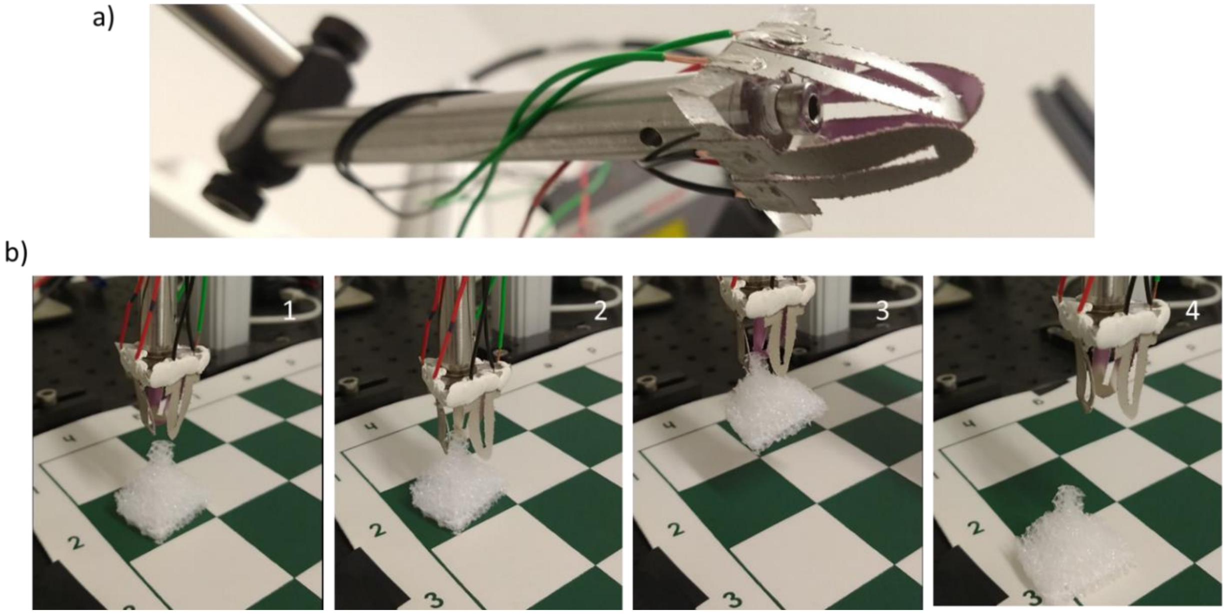

Figure S3. Gripper device. a) Image of a gripper device composed of three independent electrically active actuators **1a** as fingers. b) 1- without current the gripper approaches the target sample (ca. 100 mg), 2- simultaneous injection of electrical current in the actuators results in the opening of the gripper, 3- stopping the current flow allows catching the sample and the sample can be moved to a precise location, 4- new injection of current allows to release the object.

4-Sample characterization

Elemental analyses of C, H, and N were performed after combustion at 850 °C, by using IR detection and gravimetry by means of a Perkin–Elmer 2400 series II device. Particle size was determined by transmission electron microscopy (TEM) using a JEOL JEM-1011. TEM samples were prepared by placing on a carbon coated copper grid a drop of the particles suspended in ethanol. SEM images were acquired using a JEOL JSM 7800F Prime operated at 5 kV. Samples for SEM were prepared by breaking the film cooled by liquid nitrogen and the cross section was metalized with Pt. Variable-temperature optical reflectivity data were acquired with a MOTIC SMZ-168 stereomicroscope equipped with MOTICAM 1000 color CMOS camera. A 2 Kmin^{-1} rate was used for both cooling and heating. Thermomechanical testing was performed on a temperature controlled tensile stress stage (Linkam Scientific, TST-350). To perform constant strain testing, the first step was to set the temperature to 30 or 45 °C where the sample is equilibrated during 15 minutes. Then, we set an initial stress by increasing the clamp-clamp distance by 12 micrometers. The probe is equilibrated during 15 minutes more. Once equilibrium is achieved (no fluctuations in the registered force) the temperature cycling began. Simultaneously, a series of photos, focused on the fracture zone, were acquired at a rate of one photo per °C that allow us to track the color change associated with the spin transition. After the first temperature cycling, the sample is equilibrated before the distance between the clamps is increased again by 12 micrometers, followed by a second temperature cycle. This procedure is repeated 5 times for each sample.

5-Bilayer actuator test bench

Position tracking of the actuator devices was performed using a Micro-Epsilon opto-NCDT 2300 laser triangulation system. Current control of the samples was done by a Keithley 2420 source meter unit. The LabVIEW software was used for both controlling the sample in open-loop and closed-loop. A LabVIEW program was especially developed for the open-loop control of the sample in response to current positive steps in the range [0.9 A, 1.2 A], we have chosen because it makes possible to control the tip movement of the sample in the range [0,7 mm] which is just beyond the considered positioning range we plan to control in closed-loop. The duration of the step was tuned in order to be sure to achieve the steady state, typically between 90s and 120s. Due to the danger of damage to the sample if this one was heated for a too long period of time at a high temperature, no open-loop identification was performed beyond 1.2 A while the closed-loop control program makes possible a current control until 3 A. The closed-loop control program proposes a choice of different desired positioning signals including steps, and sine-waves with the possibility of changing both frequency and amplitudes during the movement. The PID used for the closed-loop control is the one proposed by the LabVIEW software: the output current $I(t)$ is generated according to the following equation: $I(t) = K_c[e(t) + T_d\dot{e}(t) + (\frac{1}{T_i})\int_0^t e(t)dt]$, where $e(t)$ is the position error, K_c the PID-gain whose dimension is $\mathrm{A.mm}^{-1}$ and T_d, T_i are, respectively, derivative and integral parameters in seconds. The temperature of the samples was controlled via infrared imagery with a Micro epsilon 640 Thermal Imager.

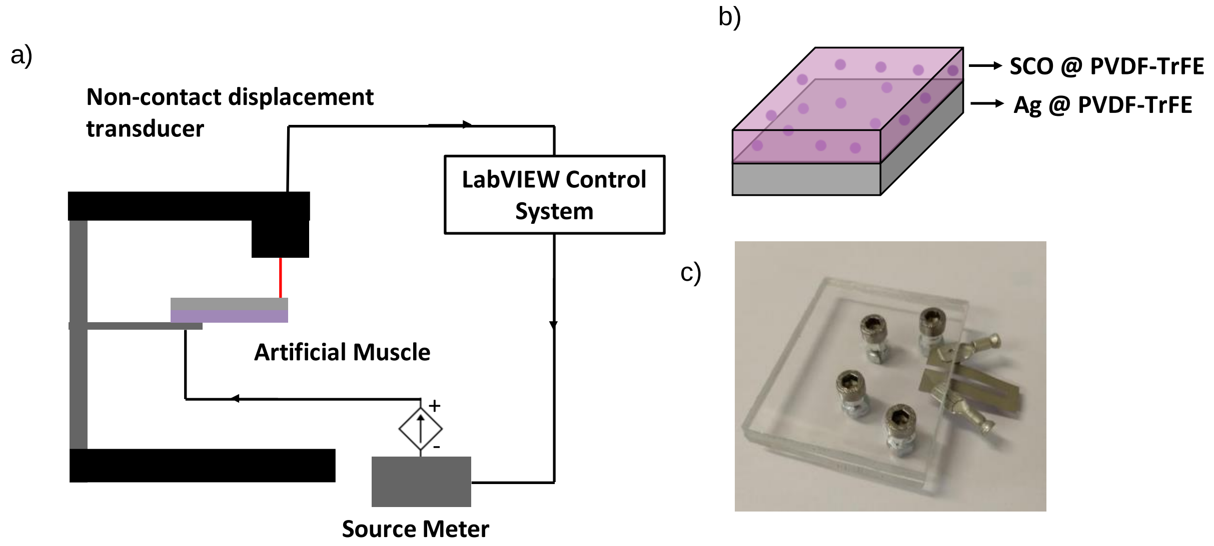

Figure S4. Experimental setup: (a) General scheme, (b) Two-layer structure defining the monolithic structure of the actuator material, (c) Photography of a sample clipped in its support.

6-Identification

Because the modelling of the bending sample was considered too complex, too difficult to do for being relevant in order to determine an efficient closed-loop control, we decided to proceed to a direct identification of the artificial muscle contraction (i.e. its "bending"). Such open-loop identification has been made possible due the natural positioning stability of the artificial muscle in response to a current step. The positioning open-loop identification was made according to the following second-order model: $x_M(s)/I(s) = K/(1+T_1 s)(1+T_2 s)$, where x_M denotes the tip position of the bending artificial muscle, I the control current, K the gain of the system, T_1 and T_2, the time "constants" of the system, supposed to be overdamped. Corresponding damping factor z and undamped natural frequency w_n were deduced from following formulas: $z = (T_1 + T_2)\sqrt{T_1 T_2}/2$ and $\omega_n = 1/\sqrt{T_1 T_2}$. The identification accuracy was simply measured by: $Mean_{\,0 \le t \le t_{horizon}} \left|(x_L(t) - x(t))/x_L(t)\right|$ where t_{horizon} is a time horizon we have taken equal to 70s. Close values were got in the considered range: 0.11mm for 0.7A, 0.07mm for 0.8A, 0.08mm for 0.9A, 0.06mm for 1A, 0.08mm for 1.1A and 0.10mm for 1.2A, which suggests a satisfactorily identification. The parameters resulting from the identification are shown in Fig. S5.

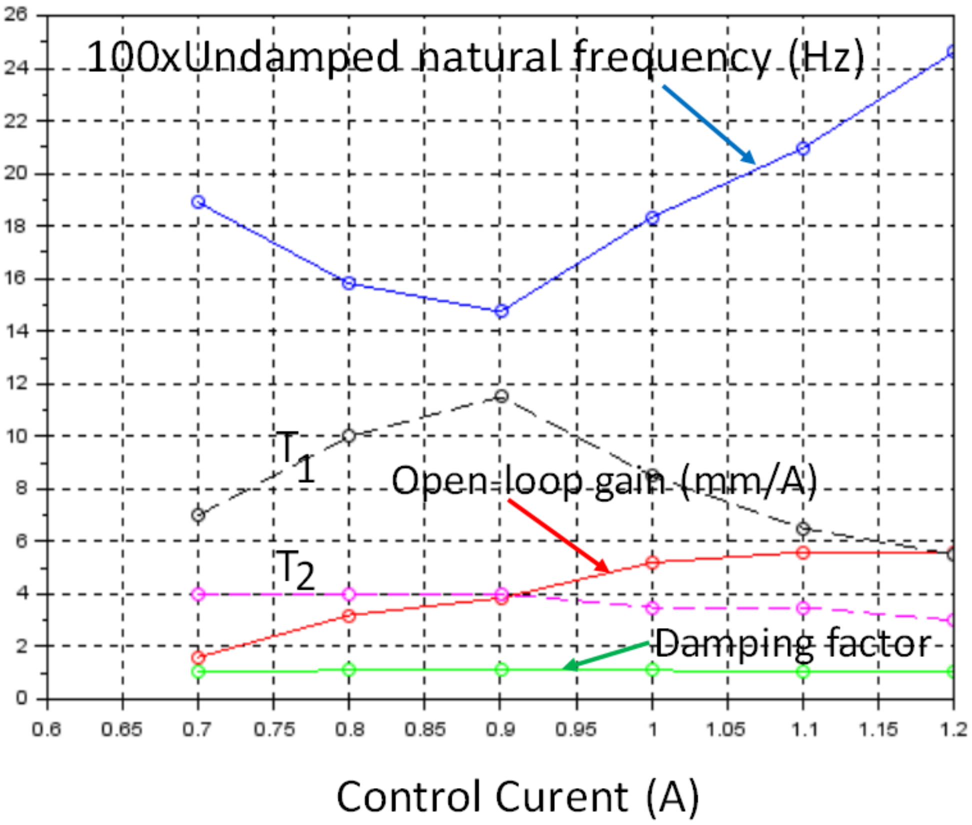

Figure S5. Second-order parameters resulting from the open-loop identification.

Actuators **1a-5a** were analysed in open loop to identify their optimal PID parameters and set up a closed loop control system. However, actuator **4a** could not be accurately assessed with the same model, as it does not undergo spin transition through the actuation process. In order to perform open loop characterization and closed loop control of actuator **5a,** the position sensor was set to capture the position of the base of the actuator, rather than the tip, as our measurement set up does not allow us to properly quantify in real time the coiling motion of sample **5a.** Representative examples of position tracking of actuators **1a**, **2a**, **3a** and **5a** under closed loop control following a sinusoidal input are shown in figure **S6**.

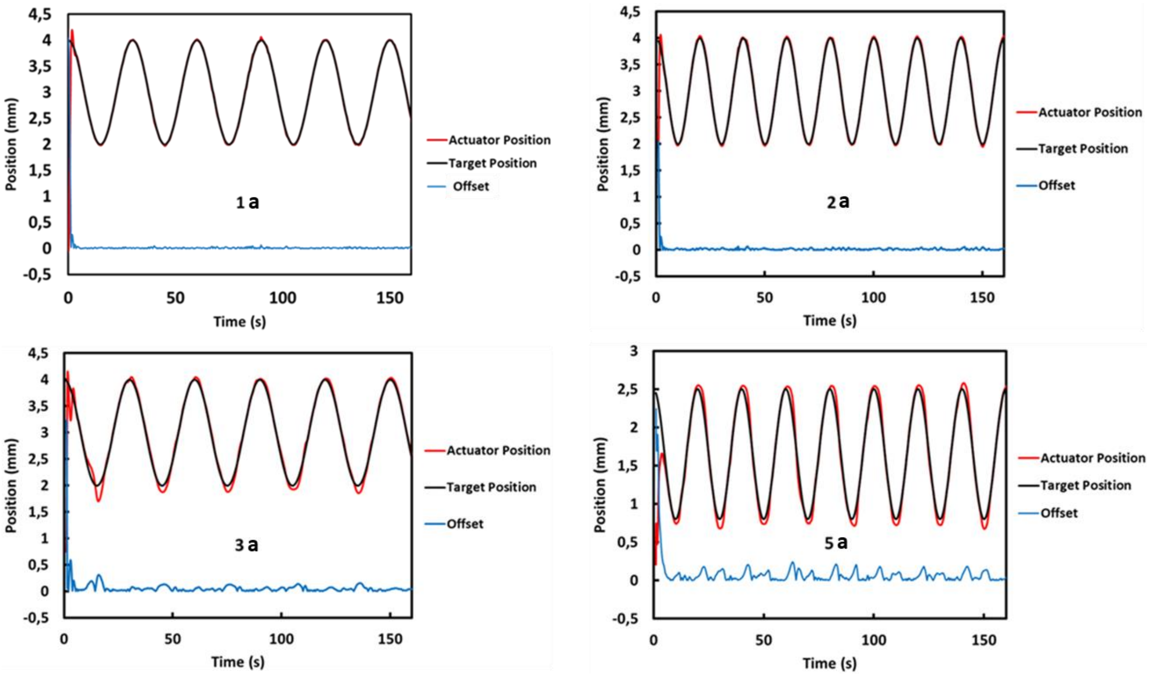

Figure S6. Closed loop control of actuators **1a-3a, 5a** for given sinusoidal inputs.

B-Electron microscopy characterization

1- Transmission electronic microscopy (TEM) of the spin crossover complexes 1 and 5

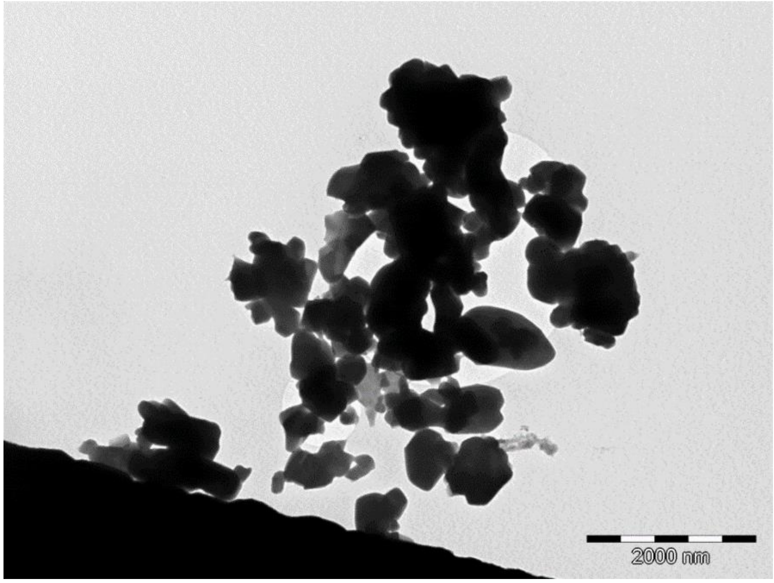

Figure S7. Representative TEM image of complex [Fe(C_5trz)$_3$](tosylate)$_2$ (**1**)

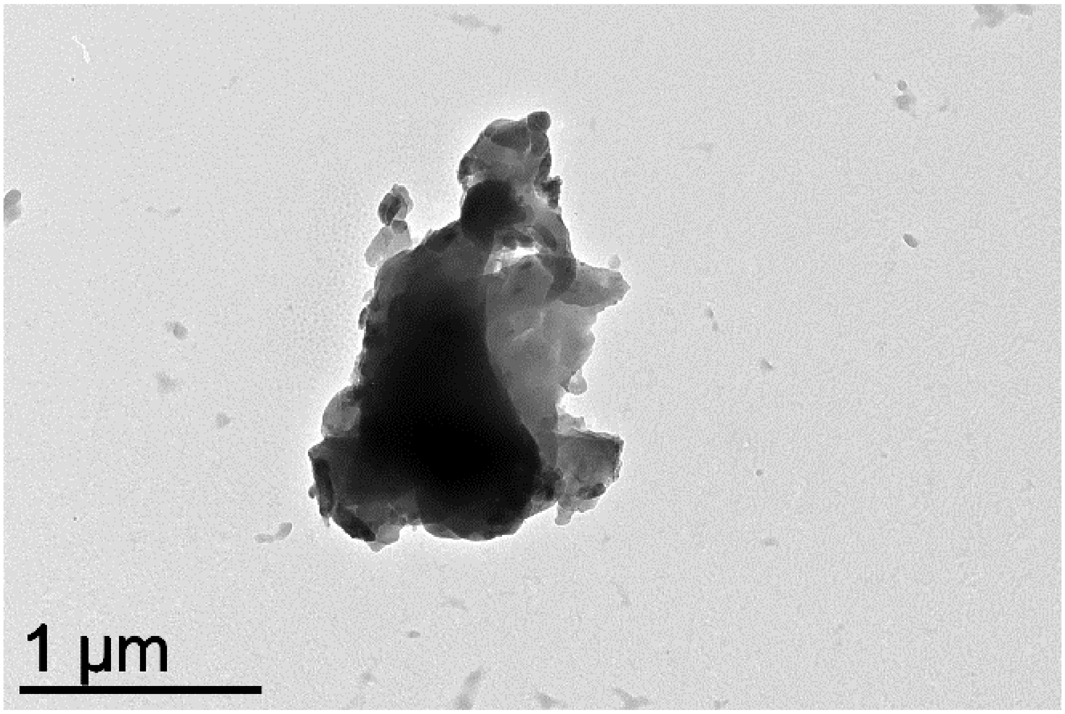

Figure S8. Representative TEM image of complex [Fe(C_{18}trz)$_3$](tosylate)$_2$ (**2**)

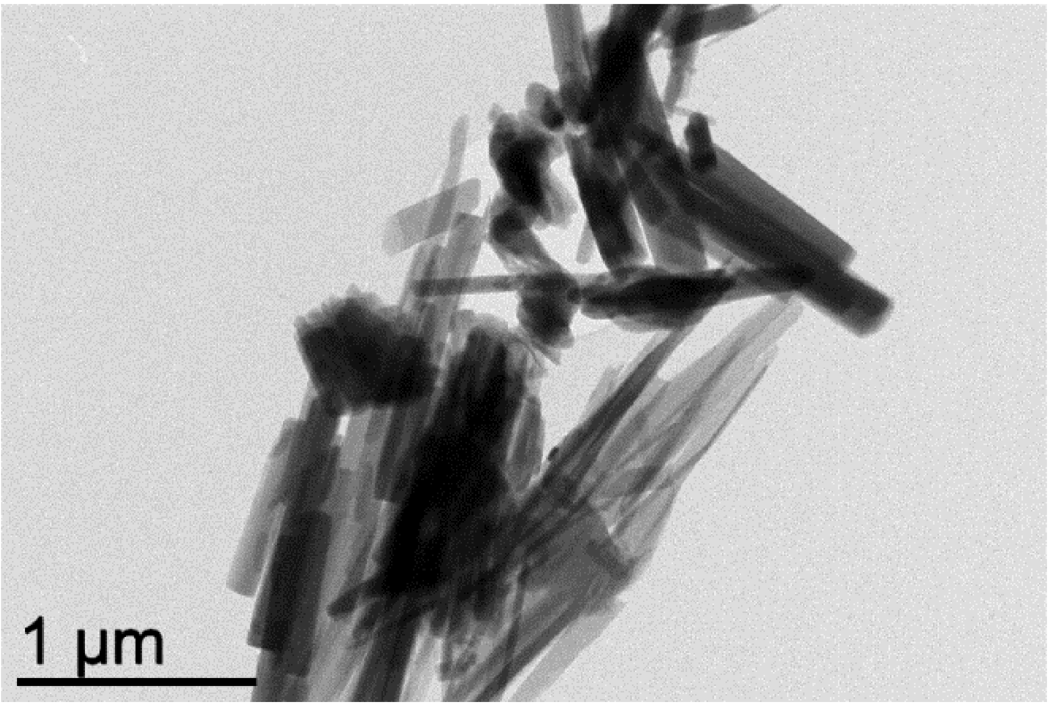

Figure S9. Representative TEM image of complex Fe(NH_2trz)$_3$$SO_4$ (**3**)

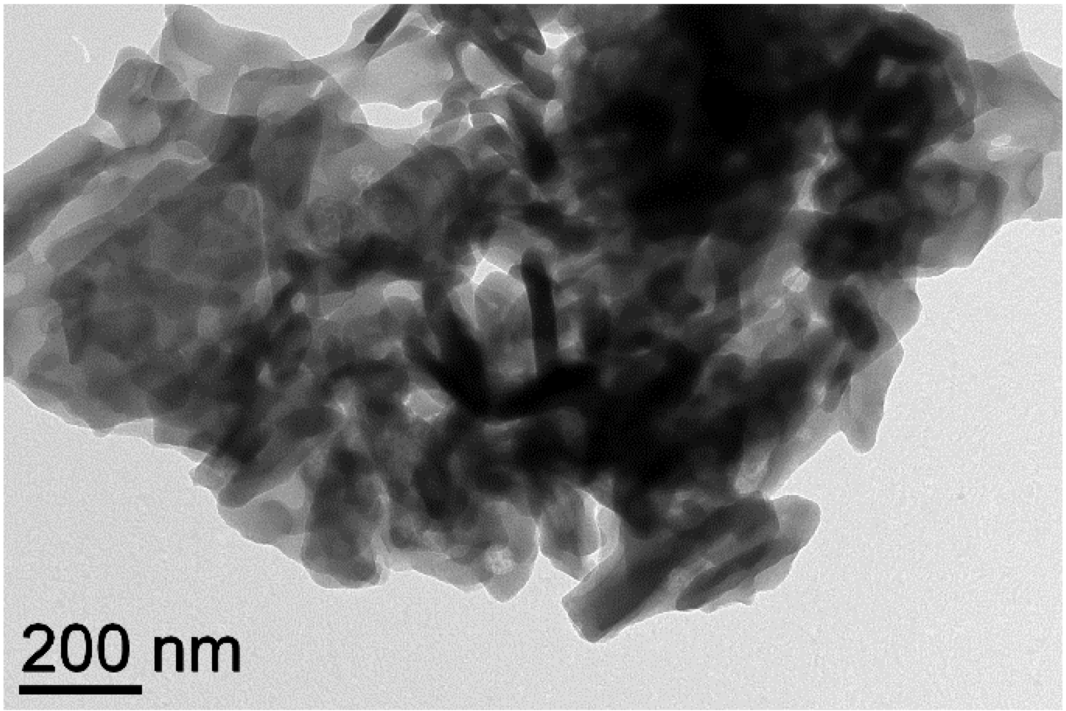

Figure S10. Representative TEM image of complex [Fe(NH_2trz)$_3$](BF_4)$_2$ (**4**)

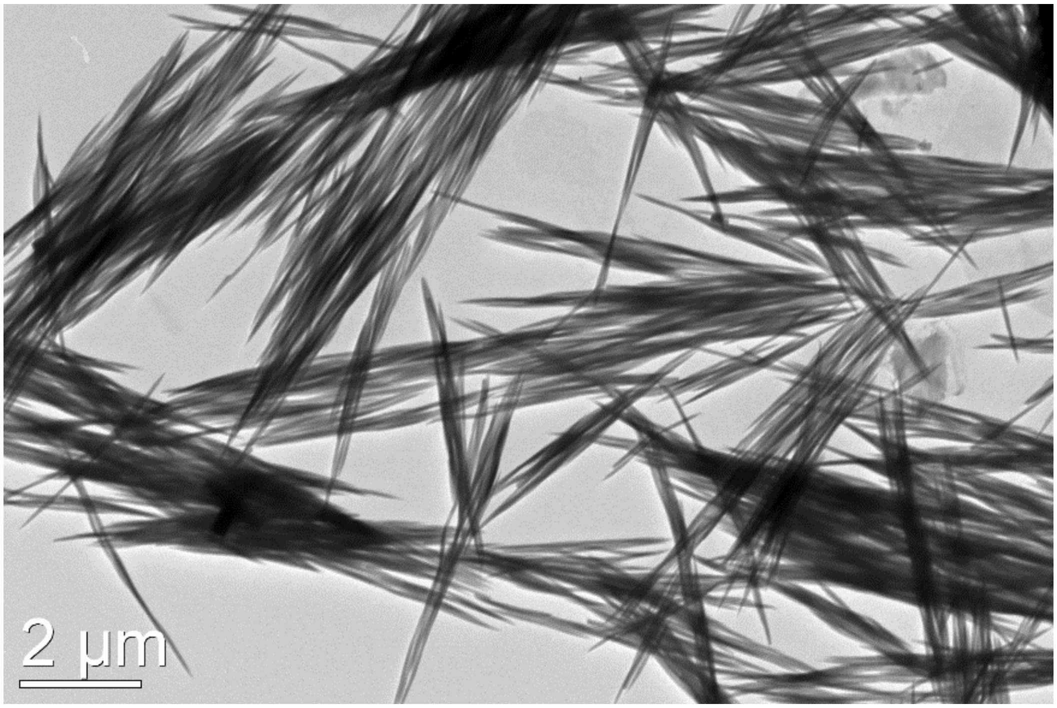

Figure S11. Representative TEM image of complex $[Fe(Htrz)_{1.8}(trz)_{1}(NH_2trz)_{0.2}](BF_4)_{1}\cdot_{0}\cdot 7H_2O$ (**5**)

2-Scanning electronic microscopy (SEM) of composite 5a

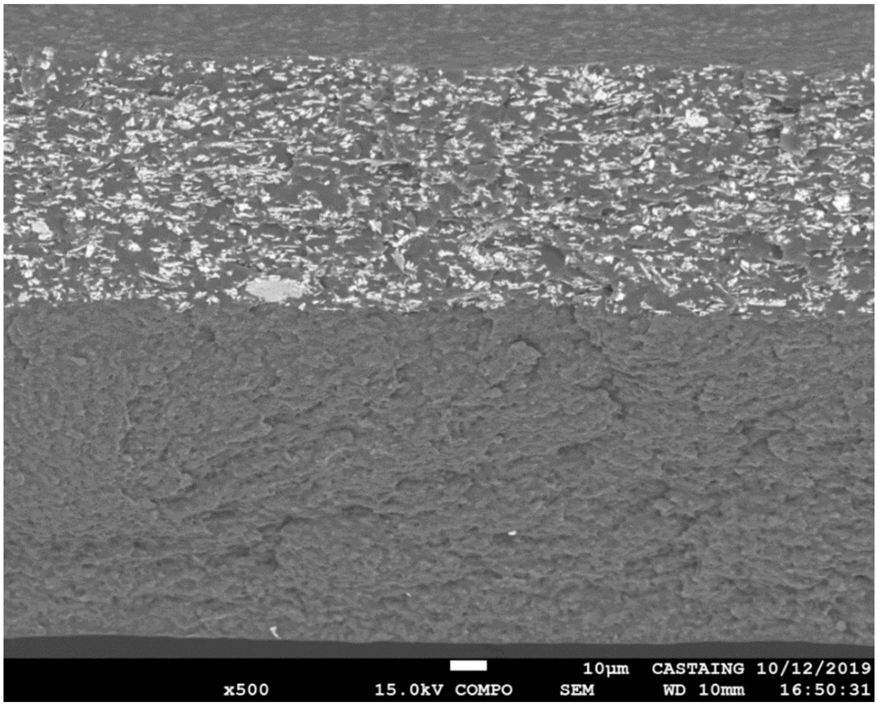

Figure S12. Cross-section of the bilayer (silver layer at the top 60 µm, SCO layer 90 µm)

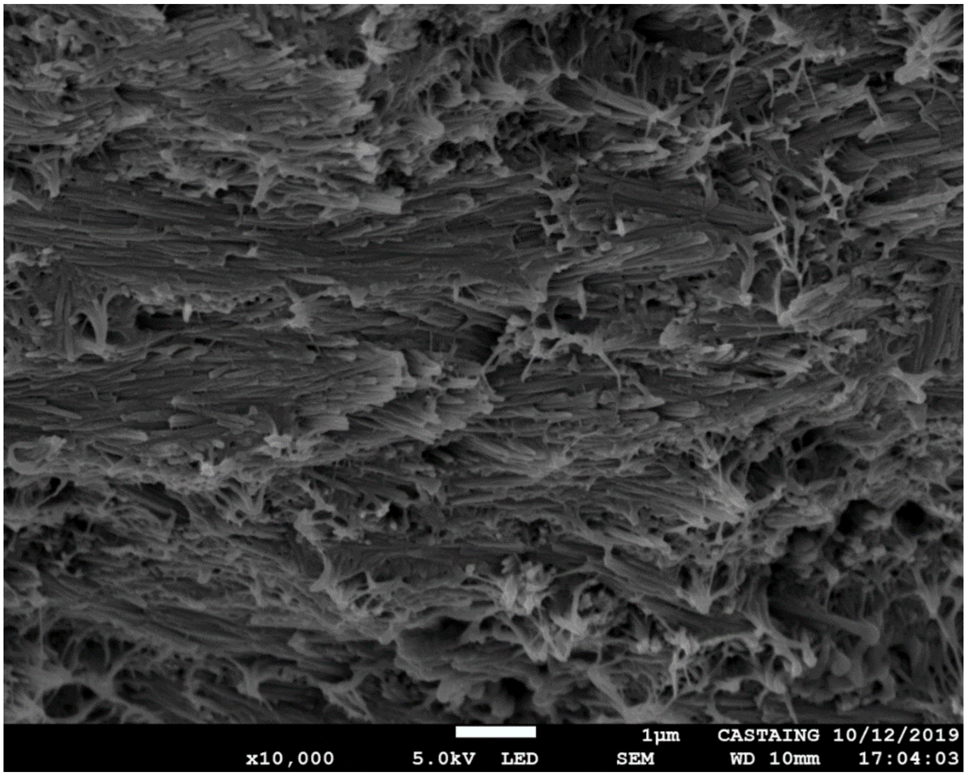

Figure S13. Parallel cross-section of the active layer

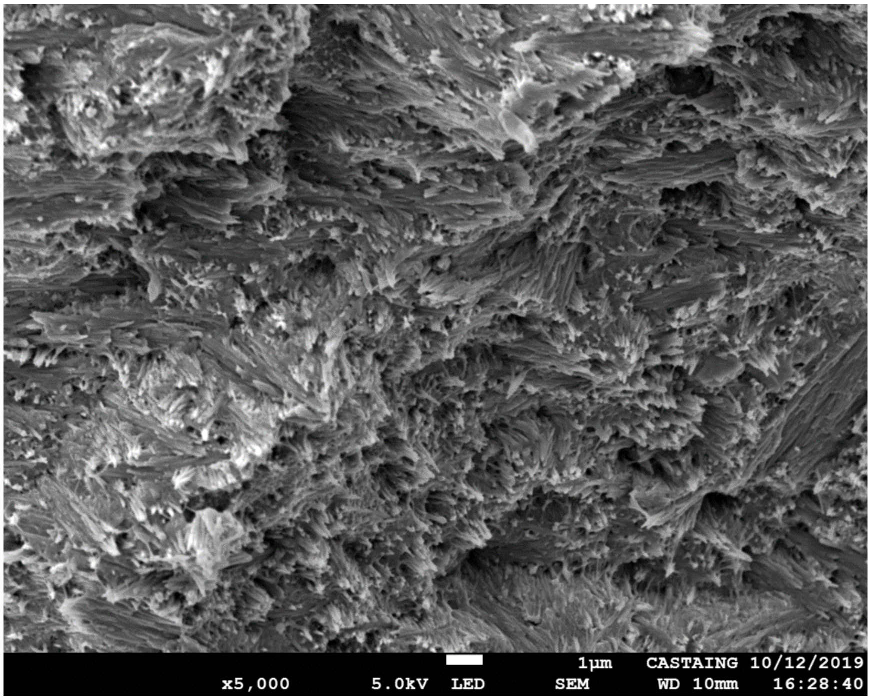

Figure S14. Perpendicular cross-section of the active layer

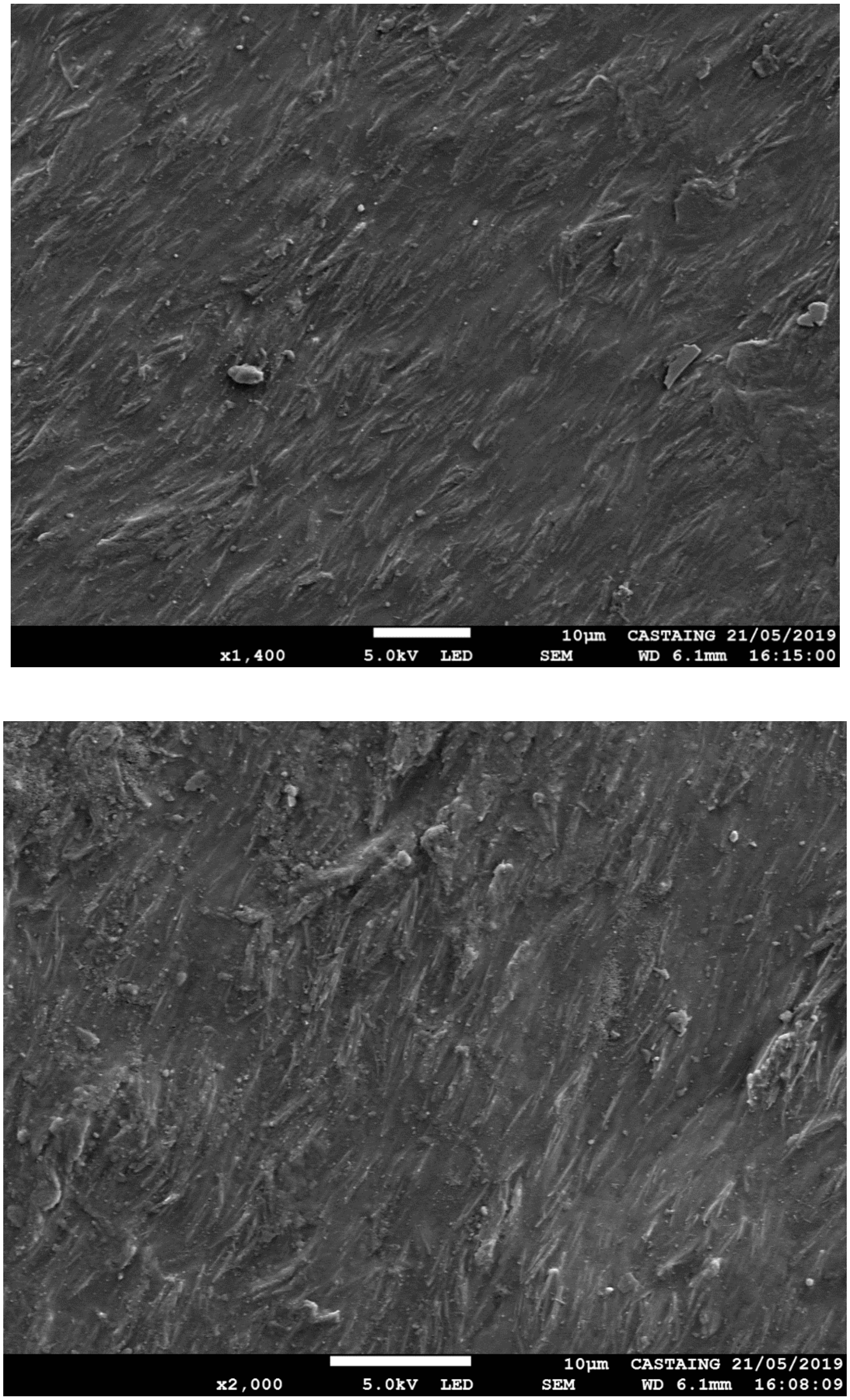

Figure S15. Surface of the active layer

3-Atomic Force Microscopy (AFM) of composites 1a and 5a

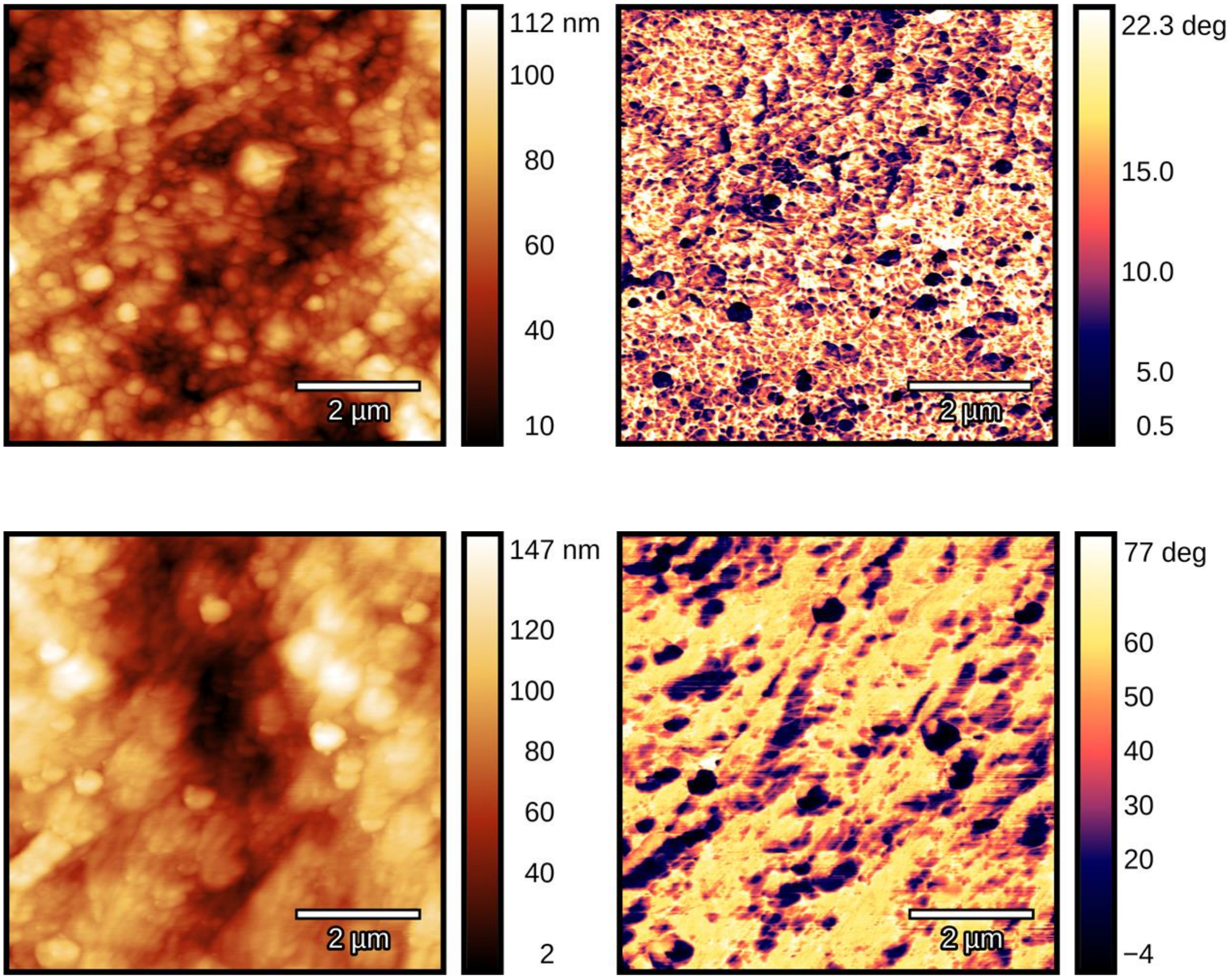

Figure S16. AFM image (topographic and phase-contrast) of sample **1a** before (top) and after (down) 35000 thermal cycles

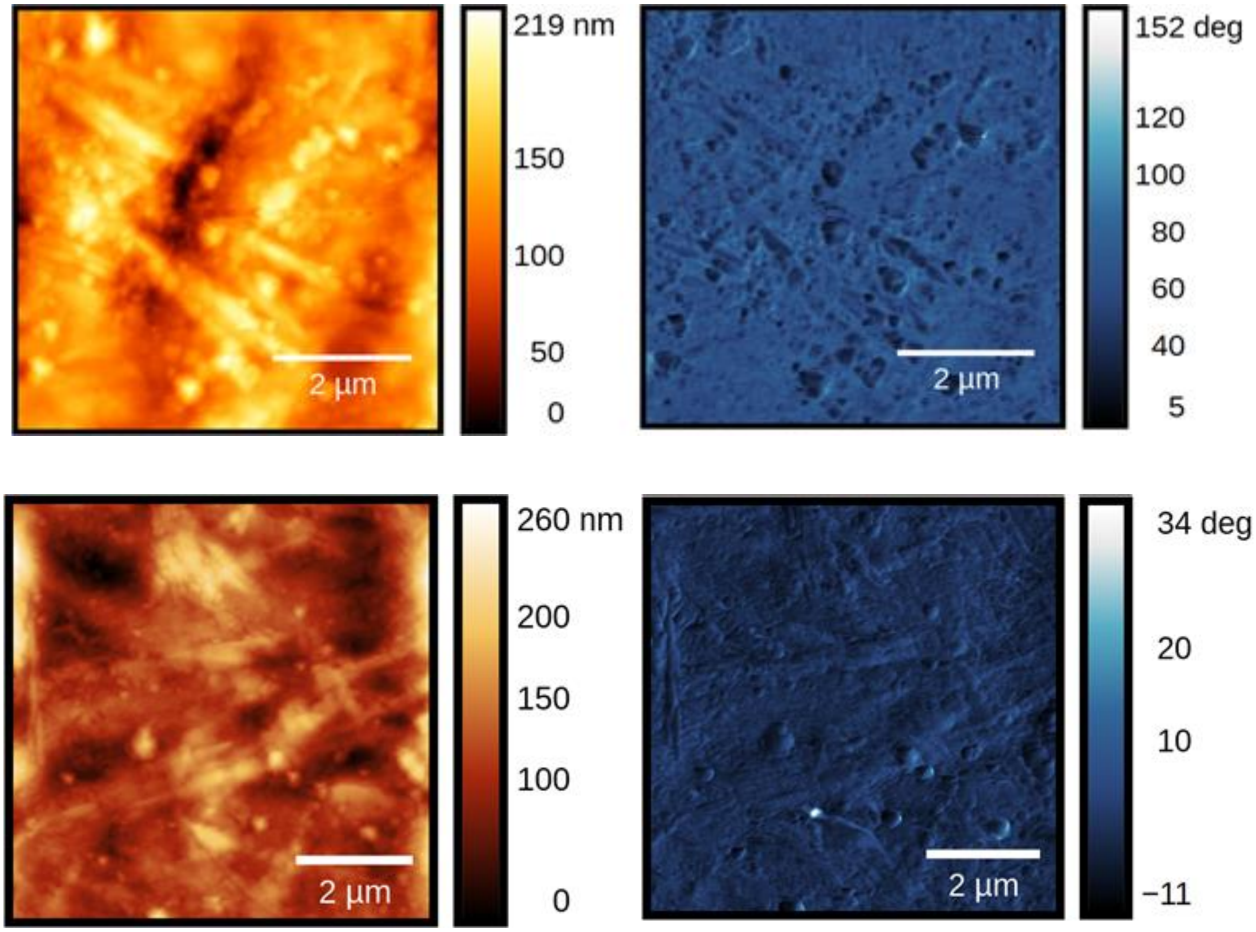

Figure S17. AFM image (topographic and phase-contrast) of sample **5a** before (top) and after (down) thermal cycles

C-Spin crossover properties

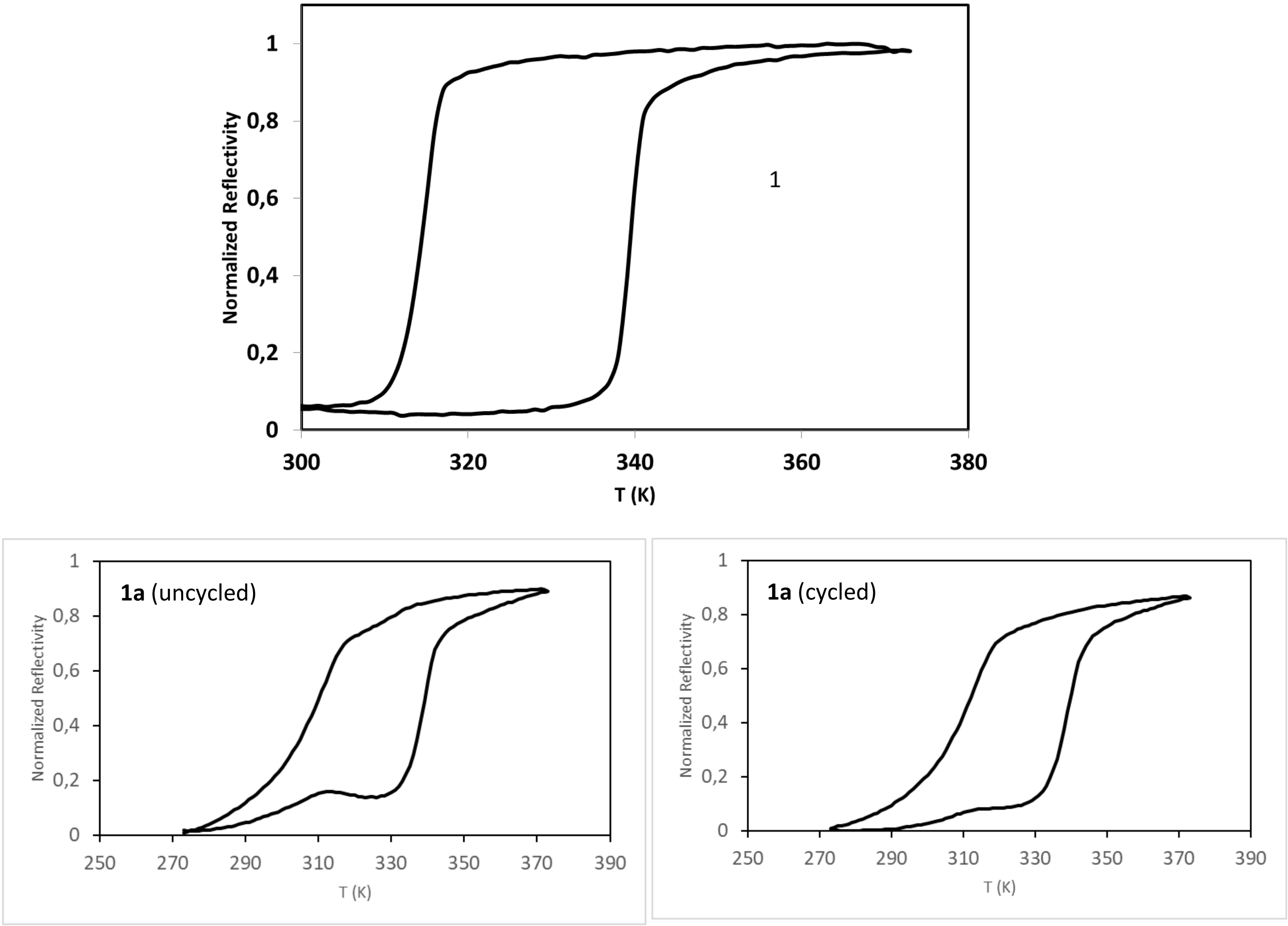

Figure S18. Variable temperature optical reflectivity measurements (second cycle) for sample **1** and bilayer **1a** (uncycled and cycled (35000 cycles) samples). Difference in the cooperative character of the transition in between the bulk and the composite samples can be explained by a matrix effect (J. Mat. Chem. C, 2020, 8, 6042-6051).

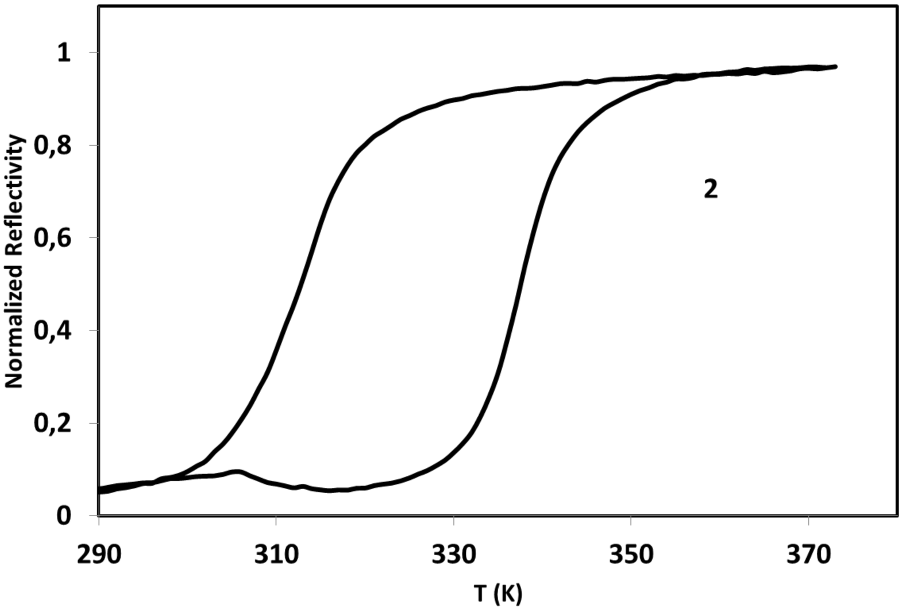

Figure S19. Variable temperature optical reflectivity measurements (second cycle) for sample **2**

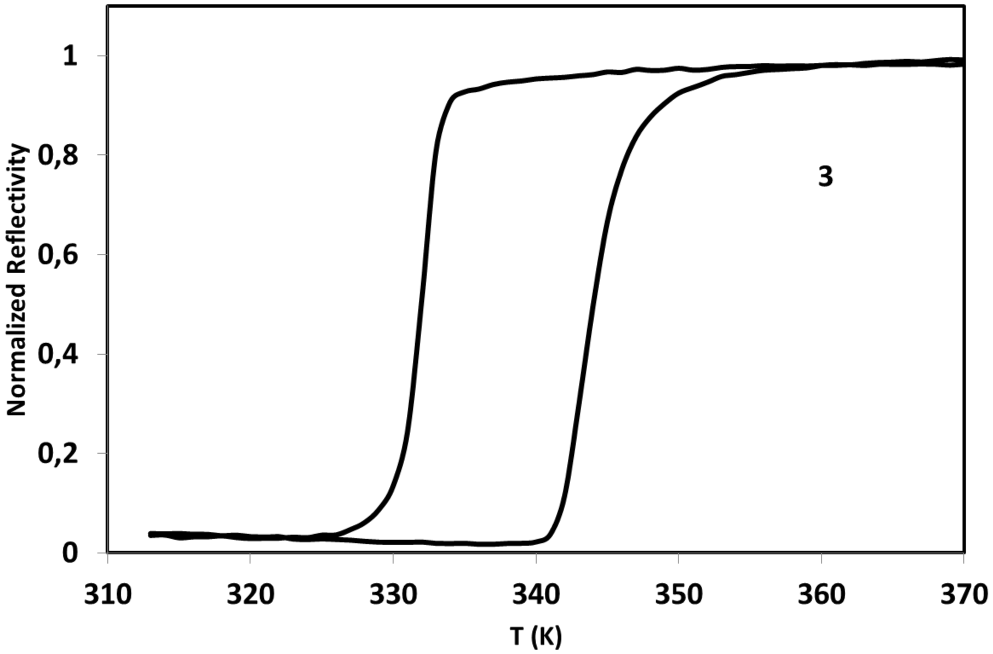

Figure S20. Variable temperature optical reflectivity measurements (second cycle) for sample **3**

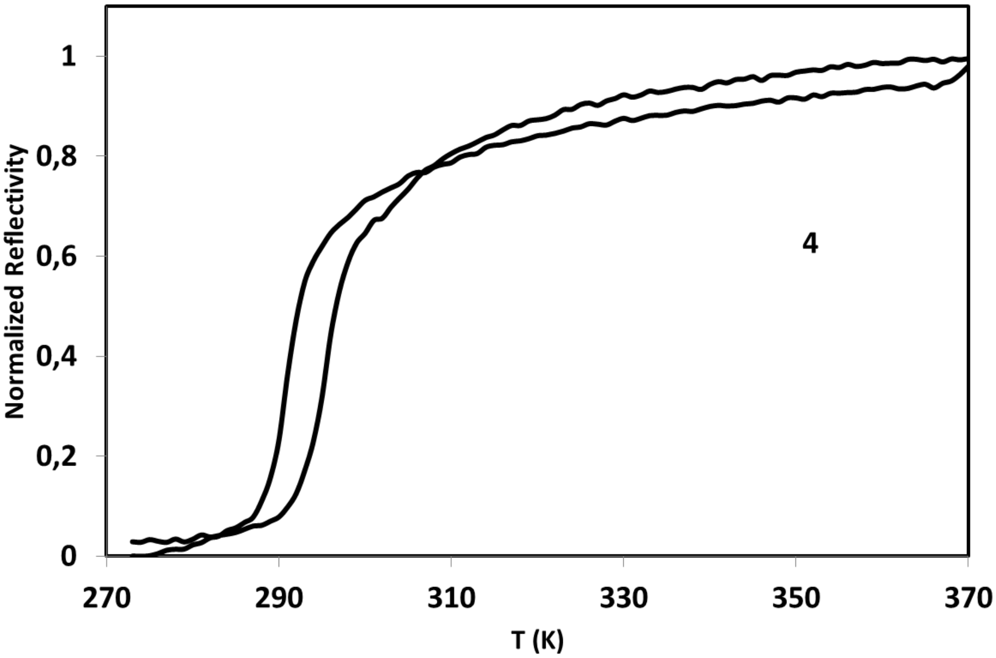

Figure S21. Variable temperature optical reflectivity measurements (second cycle) for sample **4**

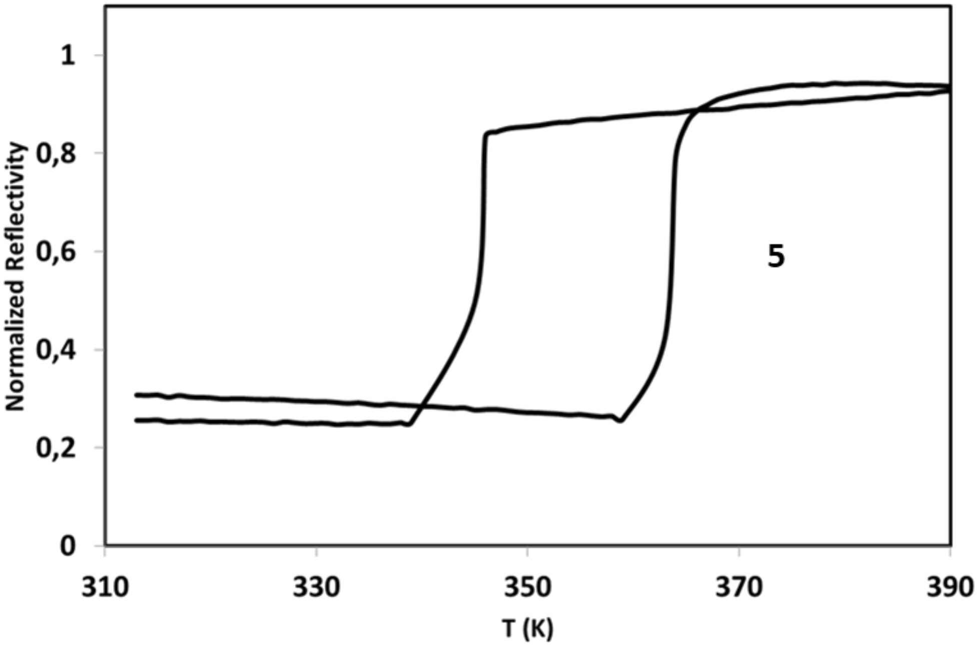

Figure S22. Variable temperature optical reflectivity measurements (second cycle) for sample **5**

D-Mechanical property analysis

Cantilever bending experiments with the bilayers 1a and 5a. Using the bilayer film fabrication method, rectangular bilayer strips were also fabricated to perform a controlled temperature measurement to assess quantitatively the actuation properties of the material using the Timoshenko beam theory equation. Samples **1a** and **5a** were compared. Sample **5a** was measured in a configuration both parallel and perpendicular to the alignment of the SCO particles in the matrix. Using Timoshenko's beam theory [J. Opt. Soc. Am. 1925, 11, 233], it is possible to associate the change in curvature k of a bilayer beam to the strain produced by the spin transition e_{SCO}:

$$k = \frac{6(\alpha_2 \Delta T + \varepsilon_{SCO} - \alpha_1 \Delta T)(1 + m^2)}{h[3(1 + m^2) + (1 + mn)\left(m^2 + \frac{1}{mn}\right)]} \tag{1}$$

with

$$m = \frac{a_1}{a_2} \tag{2}$$

$$n = \frac{E_1}{E_2} \tag{3}$$

$$h = a_1 + a_2 \tag{4}$$

where a_i is the thickness of each layer, E_i is the biaxial Young's modulus of each layer, α_i is the thermal expansion coefficient of each layer and ΔT is the temperature range of interest. The temperature range is restricted to exactly that of the SCO to isolate as much as possible the effect of the spin transition from any effects caused by the natural mismatch in thermal expansion coefficient between the two layers. The Young's modulus of each layer at the SCO temperature were obtained from mechanical tensile analysis. To calculate the biaxial Young's modulus a Poisson coefficient of 0.4 was assumed. Linear thermal expansion coefficients were likewise obtained from temperature-controlled mechanical testing. The change in curvature (k = 1/R) was calculated by graphical estimation from the following principle:

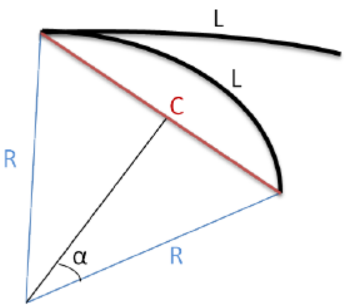

Figure S23. Graphical estimation of the curvature of a bending beam

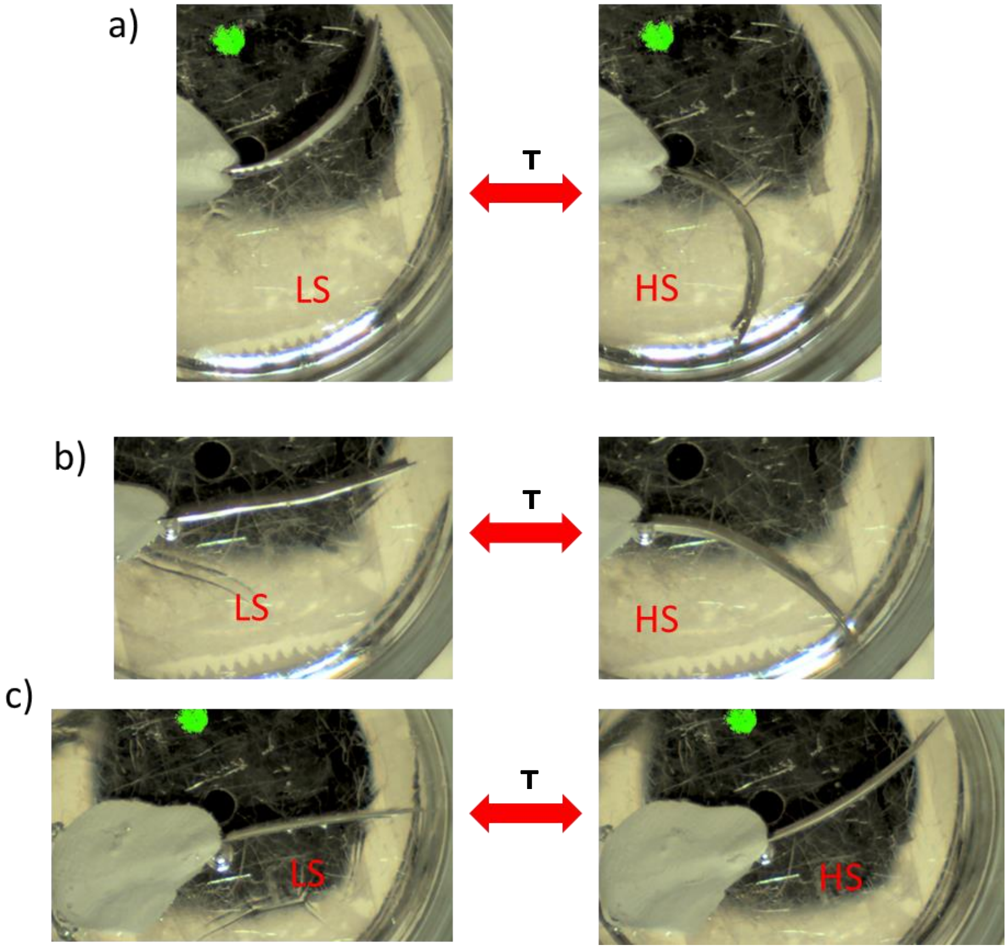

Figure S24. Movement of a rectangular bilayer strips upon the spin transition. a) Sample **5a**$_{//}$ b) Sample **5a**$_{\perp}$ c) Sample **1a**.

With these parameters, the strain of the active layer caused by the spin transition can be estimated from equation (1).

We can then calculate the volumetric work density W/V of the actuator as:

$$\frac{W}{V} = \frac{E\varepsilon^2}{2} \qquad (5)$$

Equation 1 applies only for isotropic materials, which is a reasonable approximation for the bilayer **1a,** but not for bilayer **5**. Table S1 shows the calculated data for this sample.

Table S1. Cantilever bending experiments: measured and calculated parameters

	Sample **1a**	Sample **5a**$_{//}$	Sample **5a**$_{\perp}$
k_{SCO} (m^{-1})	0.065	0.25	0.060
E SCO layer (GPa)	1.35	1.3	1.3
E Ag layer (GPa)	1.8	1.8	1.8
α SCO layer (K^{-1})	0.00054	0.00054	0.00054
α Ag layer (K^{-1})	0.00052	0.00052	0.00052
a SCO layer (μm)	137	93	93
a Ag layer (μm)	100	67	67
ε_{SCO} (%)	1.1	7.1*	1.7*
WV (J/cm^3)	0.09	3.8*	0.26*

* Values calculated from tensile analysis data

Thermomechanical analysis of composite 5a. The blade-casted composite sample **5a** was cut into 'dog-bone' shaped probes both parallel (**5a**$_{//}$) and perpendicular (**5a**$_{\perp}$) vs. the casting direction. The length and thickness of the probes were measured with a Mitutoyo Digimatic 293-805 micrometer with a resolution of 1 μm. For the thermomechanical analysis, we used a TST350E tensile stage (Linkam Scientific) with a tensile force range from 0.01 to 20 N, a maximum travel of 80 mm, force resolution of 1 mN and positional resolution of 10 μm. The TST350E has a temperature controller and a heating plate that allows heating-cooling between -195 and +350 °C with ramping at a constant rate between 0.01 and 60 °C/min and with a temperature resolution of 0.01 °C. Using this instrument, the Young's modulus of the probes was assessed by fitting the linear part of the stress-strain curves recorded at constant temperature. To determine the eigenstrain associated with the SCO (ε_{SCO}), the probes were thermalized at 45 ºC for 10 min, then clamped and the force and distance sensors were set to zero. Then, an initial tensile force was applied to the probe. Following further 10 minutes stabilization, a heating-cooling cycle was carried out at a rate of 1 ºC/min under constant force. For each probe four thermal cycles were acquired under different applied forces (0.5 – 2.0 N). The measurement output is the clamp position, from which the strain is calculated (Fig. S25). The derivative of strain vs. temperature was used to calculate the thermal expansion coefficients. The measured mechanical and actuating properties of the samples are summarized in Table S2. For comparison, the figure and the table show also the results obtained for a composite (**6a**) charged with particles of the same composition, but isotropic shape.

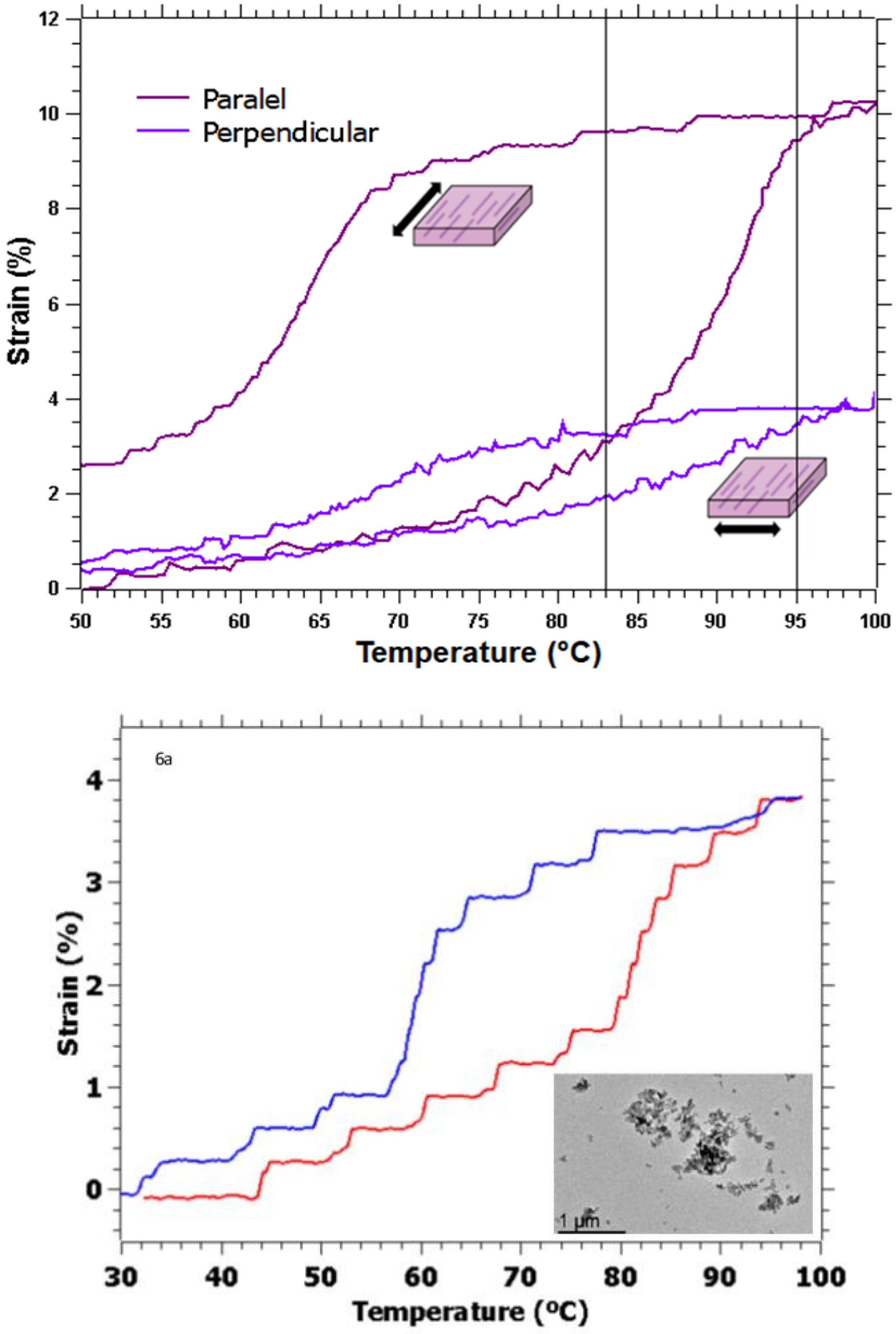

Figure S25. Thermomechanical analysis (strain vs. temperature) for the composite samples **5a** and **6a** when applying a constant tensile force of 0.5 N. For the composite **5a** the analysis was conducted both parallel and perpendicular to the preferential orientation of the needle-shaped particles. N.B. The composite **6a** was made using the same SCO complex as **5,** but with different particle morphology (ca. 50 nm mean size particles with broad size distributions and irregular shapes) resulting in an isotropic composite – in contrast to the strongly anisotropic composite **5a**.

Table S2. Eigenstrain associated with the SCO (ε_{SCO}), work density (W/V), Young's moduli (E) and thermal expansion coefficients (CTE) of the pure copolymer and the composite samples **5a**$_{\perp}$, **5a**$_{\parallel}$ and **6a**

sample	ε_{SCO} (%)	**W/V** (J/cm^3)	**E 25°C LS** (GPa)	**E 45 °C LS** (GPa)	**E 80°C LS** (GPa)	**E 80 °C HS** (GPa)	**CTE LS** (ppm/K)	**CTE HS** (ppm/K)
P(VDF-TrFE)	N/A		4.3	3.1	1.1		470	
5a$_{\perp}$	1.7	0.26	4.0	3.1	1.8	0.9	330	390
5a$_{\parallel}$	7.1	3.8	3.9	2.9	1.5	0.3	440	360
6a	1.9	0.31	3.8	2.4	1.7	0.4	270	290